Available online at www.sciencedirect.com

SciVerse ScienceDirect

Ceramics International 38 (2012) 3273–3280

CERAMICS INTERNATIONAL

www.elsevier.com/locate/ceramint

In situ growth of carbon nanotubes in alumina–zirconia nanocomposite matrix prepared by solution combustion method

A. Beitollahi [a,*], Sh. Pilehvari [b], M.A. Faghihi Sani [b], H. Moradi [a], M. Akbarnejad [c]

[a] Center of Excellence for Advanced Materials and Processing, School of Metallurgy and Materials Eng., Iran University of Science and Technology (IUST), Narmak, Farjam, Tehran, Iran

[b] Dept. of Materials Eng., Sharif University, Tehran, Iran

[c] Research Institute of Petroleum Industries (RIPI), Tehran, Iran

Received 28 May 2011; received in revised form 7 December 2011; accepted 13 December 2011
Available online 23 December 2011

Abstract

In this work successful synthesis of multiwall carbon nanotube (CNT) using solution combustion and chemical vapor deposition (CVD) methods are reported. Ceramic nanocomposite samples of $(Al_{2-x}Fe_xO_3)$–$(y)ZrO_2$ formula with $x = 0.017$, 0.034 and 0.17 and $y = 0.15$ were initially prepared. These were then subjected to CVD process during which the in situ reduction of iron oxide to metallic iron (Fe/Fe_3C) phase/s provided the necessary catalyst for the CNT formation. The formation of long flexible filaments with a smooth and regular surface bridging between alumina–zirconia (AZ) grains could be detected. The diameters of the formed filaments were in the range of ~70 to ~320 nm and length of the order of some tens of micrometers. However, transmission electron microscope (TEM) examinations also revealed the existence of small amounts of Bamboo-like carbon along with more or less straight CNTs. This could be related to the lack of strong interactions between the metallic iron phase/s and the nanocomposite support.

Keywords: CNT; Solution combustion; CVD process; Alumina–zirconia

1. Introduction

During the last decade, carbon nanotubes (CNTs) have been one of the most investigated materials due to their unique physical properties and many potential applications. This is related to their large aspect ratio (10^3–10^4) [1], high tensile strength (up to 60 GPa) [2], low density, high Young's modulus (~1 TPa) [3,4], excellent electrical conductivity and high thermal conductivity [5,6]. In this respect, ceramic–CNTs nanocomposites are reported to offer high mechanical, electrical and thermal performances compared to the conventional composite materials. Although, the homogeneous dispersion of CNTs in ceramic matrix and the set up of tight interface bonding between them is still a challenge. The latter is restricted due to the bond incompatibility between the inorganic ceramic and the covalent sp^2-bond of CNTs. Various synthesis approaches have been utilized for the synthesis of ceramic/CNTs nanocomposites such as arc discharge [7,8], laser ablation [9], catalytic CVD [10–16] and flame [17]. Fe, Ni and Co supported catalysts and short-chain hydrocarbons have been widely employed to synthesize CNTs [10–15]. It is already shown that the growth of CNTs was easier over Fe as the catalyst than over Co [11–13]. Most of previous researchers have used different metallic salt solutions to disperse Fe, Ni or cobalt catalysts on ceramic supports [14–16]. In the work reported here, we have utilized solution combustion method for the synthesis of a ceramic nanocomposite precursor of $Al_{2-x}Fe_xO_3$–$(y)ZrO_2$ ($x = 0.017$, 0.034 and 0.17, $y = 0.15$) formula. The obtained powders were then subjected to a step-like heat-treatment in different atmospheres such as argon, H_2 and CH_4 at a maximum temperature of 1000 °C to prepare CNT-alumina zirconia (CNTAZ) nanocomposites. Further, various measurement techniques such as X-ray diffraction (XRD), Raman spectroscopy as well as high resolution TEM (HRTEM) was used to characterize the obtained samples.

* Corresponding author at: Center of Excellence for Advanced Materials and Processing, Nanomaterials Research Group, School of Metallurgy and Materials Eng., Iran University of Science and Technology (IUST), Narmak, Farjam, Tehran, Iran. Tel.: +98 21 77459151; fax: +98 21 77459151.

E-mail address: beitolla@iust.ac.ir (A. Beitollahi).

0272-8842/$36.00
doi:10.1016/j.ceramint.2011.12.033

2. Experimental

2.1. Chemicals used

The following raw materials were used: Al $(NO_3)_3{\cdot}9H_2O$ (Aldrich, 99.8%), zirconyl nitrate hexahydrate ($ZrO(NO_3)_2{\cdot}5H_2O$), (Merck, 99.8%), $Fe(NO_3)_3{\cdot}9H_2O$ (Merck, 99.8%), urea ($(CO(NH_2)_2)_2$), (Aldrich, 99.8%) and cetyltrimethyl ammonium bromide (CTAB), (Merck, 99.8%) as the surfactant.

2.2. Nanocomposite preparation

As mentioned before, alumina–zirconia–iron oxide nanocomposite powders were initially prepared by solution combustion method as the initial ceramic support. This method involves the preparation of a homogeneous fuel-oxidant precursor and its exothermic decomposition [17]. The resulting powder is usually in the form of agglomerates comprising of nanoparticles as the building blocks [18]. The nominal composition of powders prepared in this work were $(Al_{2-x}Fe_xO_3)$–$(y)ZrO_2$ with $x = 0.017$, 0.034 and 0.17 and $y = 0.15$. The general theoretical stoichiometric equation for the formation of the prepared nanocomposite powder was considered as:

$$a(Al(NO_3)_3) + b(ZrO(NO_3)_2) + x(Fe(NO_3)_3) + d(CH_4N_2O) \rightarrow (Al_{2-x}Fe_x)O_3 \cdot bZrO_2 + \beta H_2O + \kappa CO_2 + \theta N_2 \quad (1)$$

where *a*/*b* molar ratio was 15/85. It should be noted that, for a stoichiometric combustion reaction between a fuel and oxidizer, the ratio of the net oxidizing valency of the metal nitrate to the net reducing valency of the fuel should be equal to one [18]. In this regard, carbon and hydrogen are considered as oxidizing element with the valency 2 and 1, respectively and nitrogen is assumed to have a valency of zero. The total reducing valency of urea was 6. To prepare the initial precursor powders, the required amounts of the raw materials were initially weighed with an accuracy of 0.1 mg. These were then separately dissolved in minimum amounts of distilled water under continuous stirring to form a clear solution. Thermal dehydration of the urea-nitrate solutions on a hot plate at ~80 °C resulted in a transparent viscous gel. For the samples with fuel to oxygen ratio (F/O) equal to 1 the obtained gel on further heating at ~250 °C swelled and self-ignited for about 5 s with rapid evolution of large volume of gases and produced voluminous powder. However, for the sample with F/O ratios of 0.8 and 1.2, i.e. below and above the stoichiometric ratio (F/O = 1) comparatively slower ignitions happened. Therefore, all of samples were prepared with F/O ratio of unity. Further, the prepared samples were later also calcined at 1150 °C for 2 h in air to convert the obtained metastable alumina phases into stable α-alumina phase as will be discussed later. The calcined sample was then subjected to high energy vibrating milling (Spex 8000) in a hardened steel vial with steel balls for 15 min to break the flaky agglomerates formed.

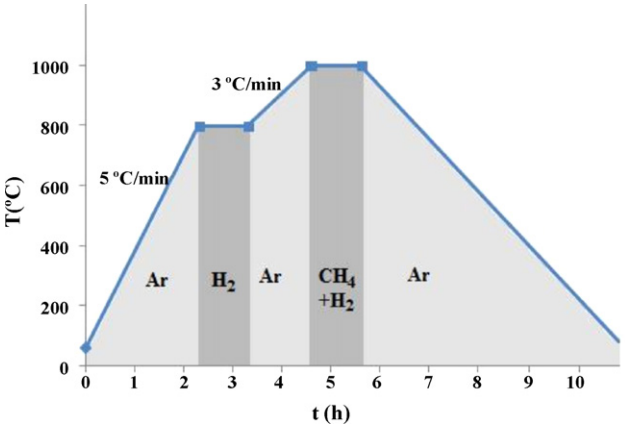

Fig. 1. Heat treatment schedule applied for the synthesis of CNTAZ samples in different gas/gas mixture atmosphere/s.

2.2.1. Carbon nanotube growth

CNTAZ composites were prepared by CVD method. In this respect, previously milled samples were subjected to a step-like heat treatment at a maximum temperature of 1000 °C for 1 h in various atmospheres such as argon (Ar), hydrogen (H_2) and methane (CH_4) as shown in Fig. 1. In this respect, the initial milled precursor powders were heated to reach 800 °C in pure argon atmosphere with a heating rate of 5 °C/min. The argon gas flow was then replaced by a gas mixture of H_2 and argon (400 cm^3/min) and the samples were kept at this temperature for 1 h. Then in the next step, the gas atmosphere was switched to pure argon gas (200 cm^3/min) and the samples were heated up to 1000 °C with a heating rate of 3 °C/min. This was followed by soaking the specimens for 1 h in gas mixtures of CH_4–H_2 atmosphere (100, 400 cm^3/min). Finally the samples were furnace cooled to room temperature in pure argon atmosphere (Fig. 1).

2.3. Characterization

XRD patterns (Cu $K\alpha_1$) were recorded in the range 10–80° (2θ) with a Philips diffractometer (JEOL-JDX-8030). Working voltage and current were 40 kV and 80 mA, respectively. Microstructural studies on the synthesized powders were carried out both by SEM (Philips) and TEM (Philips, CM200) techniques. Raman spectra were also recorded using an Almega-Thermo-Nicolet spectrometer (532 nm). Spectroscopic analyses of the prepared samples were also performed using Fourier transform infrared (FTIR) spectrometer (Bruker, Vector 33). In order to measure carbon yield, weight gain measurements were conducted. In this respect, the yield was defined as the weight gain ratio of the synthesized powder containing carbon filaments/CNTs to the initial precursor powder used.

3. Results and discussion

Fig. 2 demonstrates XRD multiplot patterns of different as-ignited powder samples prepared by solution combustion

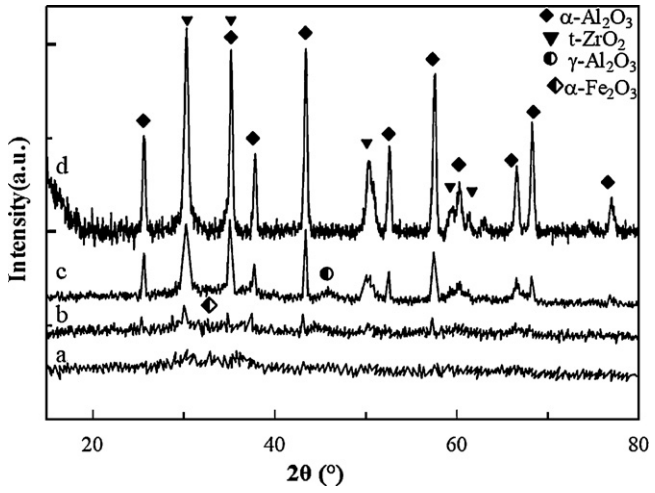

Fig. 2. XRD multiplot of the as-ignited alumina zirconia precursor powders with $x = 0.17$ (a), 0.034 (b) and 0.017 (c). XRD pattern of the sample with $x = 0.017$ (d) after calcinations at 1150 °C for 2 h.

method as well as the sample with $x = 0.017$ calcined at 1150 °C for 2 h. As can be realized from this figure, for the sample with $x = 0.17$ no signs of crystallization was noticed evidenced by the presence of a broad and rising background. However, by increasing the level of iron nitrate content, higher degrees of crystallinity could be noticed. For the sample with $x = 0.034$, early signs of crystallization was noticed with the presence of hematite (α-Fe_2O_3), γ, α-alumina and tetragonal zirconia (*t*) phases. In case of the sample with $x = 0.017$, the existence of strong diffraction peaks related to α-alumina and *t*-zirconia along with minor amounts of γ-alumina could be clearly identified. However, the existence of hematite phase could not be detected for this sample within the phase detection accuracy of XRD technique suggesting the possible substitution of Fe^{3+} (0.64 Å) for Al^{3+} (0.53 Å) due to their rather close ionic radii. Different authors have studied Al_2O_3–Fe_2O_3 system. The maximum solubility limit of Fe_2O_3 in α-alumina at temperatures below 1200 °C is estimated to be near 10 mol% [19–24]. As mentioned before, the comparison of XRD patterns (Fig. 2) of the as-ignited samples highlights the fact that the higher was the magnitude of *x*, the higher were the degree of crystallinity of the phases formed. It is well known that the enthalpy of combustion can be expressed by [25]:

$$\Delta H = \left(\sum n\Delta H_p\right) - \left(\sum n\Delta H_r\right) = \int_{T_0}^{T_f} \left(\sum nC_P\right) dT \qquad (2)$$

where n is the number of the mol, C_p is the specific heat capacity, T is the adiabetic flame temperature in this equation. Further, H_p and H_r are also the magnitudes of the relevant products and reactants enthalpies, respectively. Table 1 demonstrates the magnitudes of the enthalpies of different compounds used in the initial solution. Fig. 3 also compares the magnitudes of the combustion enthalpies of the precursor powders with different values of x estimated using Eq. (2). As can be noticed from this figure, the higher was the value of *x*, the lower was the magnitudes of combustion enthalpies. A similar trend could be also expected for the adiabetic temperature as well. This is also justified with XRD results obtained for the as-ignited samples (Fig. 2). As mentioned before, lower degree of crystallinity was obtained for the samples of high iron content.

Table 1
Thermodynamic data used for the calculation of combustion enthalpies of the prepared precursor.

Compound	H_f (kcal mol^{-1})	C_p (cal (mol K)$^{-1}$)[a]
$Al(NO_3)_3 9H_2O$ (c)	−857.59	
$CO(NH_2)_2$ (c)	−56.33	
Al_2O_3 (c)	−399.09	$28.062 + 0.01038T$
CO_2 (g)	−94.051	$10.34 + 0.00274T$
N_2 (g)	0	$6.5 + 0.0010T$
O_2 (g)	0	$5.92 + 0.00367T$
H_2O (g)	−57.796	$7.20 + 0.0036T$
Fe_2O_3(C)	−198.5	$24.72 + 0.01604T - 423400/T^2$
ZrO_2	−258.5	$11.62 + 0.01046T - 177700/T^2$
$Fe(NO_3)_3{\cdot}9H_2O$	−328.3	45.751
$Zr(NO_3)_2{\cdot}5H_2O$	−456.08	

(c): crystalline; (g) gas; *T*: absolute temperature.
[a] Calculated from the discrete values.

Further, as mentioned before, it is interesting to note that the formation of *t*-zirconia phase was confirmed for the sample with $x = 0.017$ and $x = 0.034$ (Fig. 2). For the latter, the crystallite sizes of the ZrO_2 and Al_2O_3 phases estimated by Scherrer method [26] were 29 and 21 nm, respectively. It is well known that ZrO_2 has three polymorphs of $P2_1/c$ monoclinic (m), $P4_2/nmc$ tetragonal (t), and $Fm3m$ cubic (c) crystal structures, with m-zirconia the equilibrium bulk structure at room temperature [27–29]. Bulk m-zirconia transforms to t- or c-ZrO_2 at 1170 °C or 2370 °C, respectively. Various attempts have been made to stabilize the c- or t-ZrO_2 to exist at room temperature by doping small amounts of different dopants such as Y_2O_3, MgO, CaO, CeO_2, AlN, Mg_3N_2, Si_3N_4, and Al_2O_3 [30–34]. These additives are believed to control the c- or t-ZrO_2 nucleation and growth in small crystallites through their total surface strain/free energy [31,34,35]. It should be also added that the process depends on the solubility of these dopants in c- or t-zirconia and the chemistry of the stabilizer used. Some of the mentioned dopants segregate to form grain boundaries and

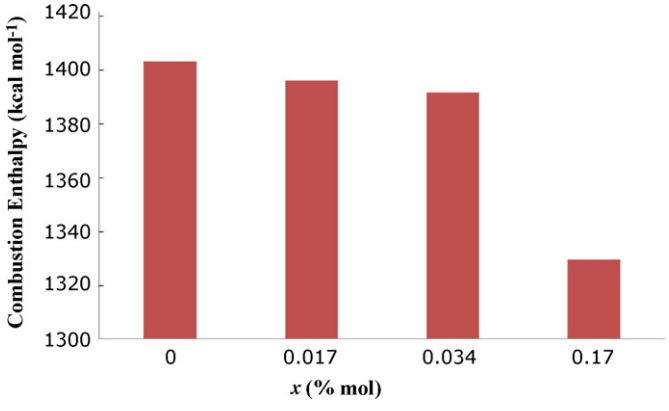

Fig. 3. Comparison of the combustion enthalpies of the various as-ignited samples prepared with different *x* [24].

part of them substitute in Zr^{4+} lattice sites giving rise to lattice strain due to cation size mismatch and creation of oxygen vacancies to compensate the electronic charges and hence increasing the total energy of the system required for the room temperature stabilization of the high energy meta-stable c- or t-zirconia phases [36]. Three forms of stabilized zirconia are generally seen: a fully stabilized one containing only c-ZrO_2 phase, a partially stabilized ZrO_2 containing t-zirconia grains in c-ZrO_2 matrix, and the third one the so-called t-ZrO_2 poly-crystals comprising of fine t-ZrO_2 grains [37]. The stabilization of the zirconia is also shown to be related both to size effect [38] and the presence of aluminum ions on the surface of the zirconia particles [39]. The latter is believed to reduce the surface enthalpy and hence increases the stability region of the tetragonal phase. The formation of t-zirconia phase for the samples prepared in this work is believed both attributed to the size effect and the existence of Al^{3+} cations surrounding zirconia particles.

As mentioned before in experimental section, the as-ignited samples were calcined at 1150 °C for 2 h in air atmosphere to convert the observed meta-stable γ to α-alumina phase. The obtained XRD pattern for the sample with $x = 0.017$ (Fig. 2) was typical for the other calcined samples (not shown here) as well. As can be noticed from this figure, the formation of α-alumina as well as t-zirconia phases with average crystallite sizes of 30 nm, and 40 nm were detected, respectively. It is already mentioned that the transformation of the metastable γ to α-alumina phase is attributed to the grain/crystallite size growth [40]. Fig. 4 shows the XRD pattern of the sample with $x = 0.017$ subjected to heat-treatment in different atmospheres as mentioned in experimental section. As can be noticed from this figure, the existence of various phases such as α-alumina, t-zirconia, α-hematite, α-Fe, Fe_3C (cementite), as well as CNT/graphite phases could be detected. It should be mentioned that the precise discrimination of α-Fe and Fe_3C is rather difficult because of the overlap between some of their respective diffraction peaks. Further, the formation of γ-Fe cannot be ruled out. Since its main diffraction peak (1 1 1) could be masked by α-alumina peak. Previous studies have confirmed the formation of this phase by Mössbauer spectroscopy technique [41] for CNT composites. The possible formation of γ-Fe/α-Fe/Fe_3C phases reflect the effect of applied reducing atmospheres during final heat-treatment step. In fact, the reduction of the prepared precursor in H_2, H_2/CH_4 atmosphere has led to the formation of Fe and Fe_3C particles that act as active sites for the decomposition of CH_4 giving rise to the production of CNT composite powder. The nucleation of filamentous carbon requires a supersaturation of carbon in iron followed by a phase transformation of the starting iron into Fe_3C and precipitation of carbon layers at the metal support interface to yield CNTs. The formation of Fe_3C phase has been also reported by others as well [42,43]. The Fe_3C phase has been known to be an active phase for the CNTs formation [44]. It should be mentioned that methane (CH_4) is known as one of

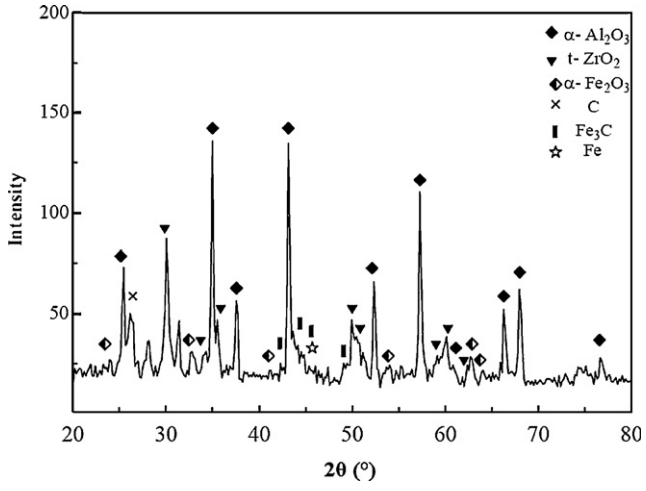

Fig. 4. XRD pattern of the CNTAZ sample with $x = 0.017$% subjected to heat-treatment in different atmospheres (shown in Fig. 1).

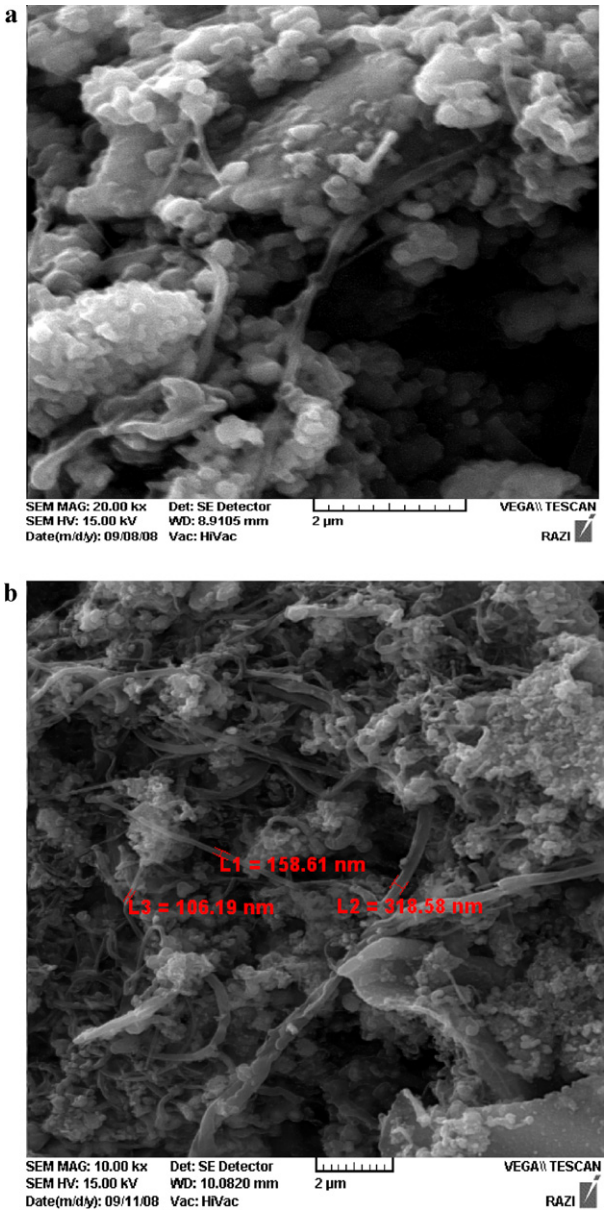

Fig. 5. SEM micrographs of the CNTAZ samples with $x = 0.17$ (a) and 0.017 (b), respectively.

the most kinetically stable hydrocarbon that undergoes the least pyrolytic decomposition at high temperatures (1000 °C) for the synthesis of the CNT nanocomposites. Therefore, the carbon atoms required for nanotube growth could be supplied by the catalytic decomposition of methane on transition metal surfaces. This would also limit the formation of amorphous carbon generated by self pyrolysis of methane. SEM micrographs of the prepared CNTAZ composite powders with $x = 0.017$ and $x = 0.17$ are illustrated in Fig. 5(a) and (b). As can be seen from these micrographs, the formation of long flexible filaments with a smooth and regular surface bridging between oxide grains could be detected. All of these filaments had diameters between ~70 and ~320 nm and length of the order of some tens of micrometers. Further, Fig. 6 also displays the typical energy dispersive X-ray (EDX) analysis obtained from different areas of the CNTAZ samples confirming the existence of different metal oxides along with carbon containing species as well as Au. The latter is related to the applied coating layer for the SEM examinations. Fig. 7(a) and (b) also demonstrates the TEM micrographs of the multiwall CNTAZ composite sample with $x = 0.017$. Raman spectroscopy results also confirmed the formation of multi wall CNTs along with amorphous carbon. Fig. 8 displays Raman spectra of the heat-treated samples with $x = 0.017$, 0.034 and 0.17 without applying any further purifications. As can be understood from this spectra the high frequency range between 1200 and 1800 cm^{-1} showing the D band (~1350) and the G band (~1582). Table 2 also summarizes the magnitudes of the intensities of D and G bands as well as their ratios for different samples studied. For the sample with $x = 0.017$, the lowest ratio of I_D/I_G was obtained. An increasing ratio of I_D/I_G value is attributed to the existence of sp^3-like carbon reflecting the existence of higher level of structural order [44]. Further, SEM observations also showed that some of the formed tubes were bent possibly due to the existence of defects occurring during the growth leading to a change in the growth direction. TEM examinations of the samples revealed the existence of small amounts of Bamboo-like carbon along with more or less straight CNTs (not shown here). This could be related to the lack of strong interactions between the metallic iron phase/s and the nanocomposite support. Ermakova et al. [45] have reported that during the synthesis of multi wall CNTs over iron supported on TiO_2 several types of carbon nanofilaments, i.e. straight, bamboo-like or nanoparticles were observed. On the other hand, when TiO_2 was replaced by SiO_2 a smaller number of bamboo-like carbon structures were formed. This was attributed to the interaction between the active phase and the support. Fig. 9(a) and (b) highlights the tip formation for the

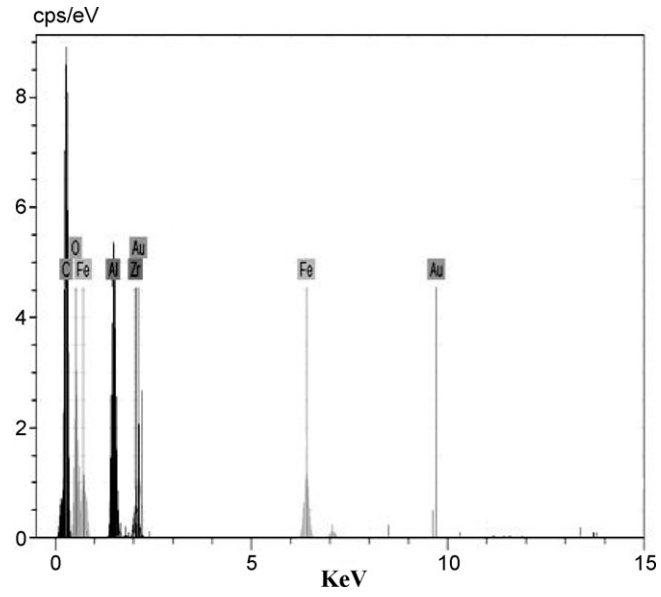

Fig. 6. Typical SEM-EDX analysis spectra of the CNTAZ sample with $x = 0.017$.

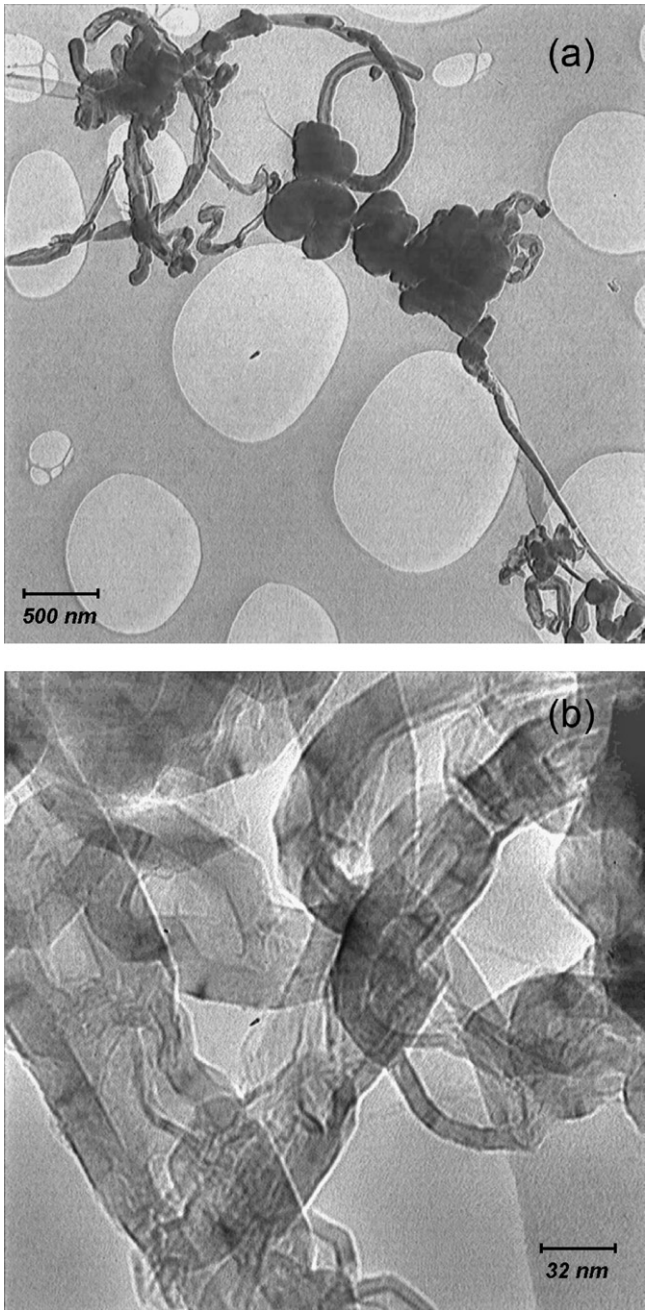

Fig. 7. (a and b) TEM micrographs of the CNTAZ sample with $x = 0.017$%.

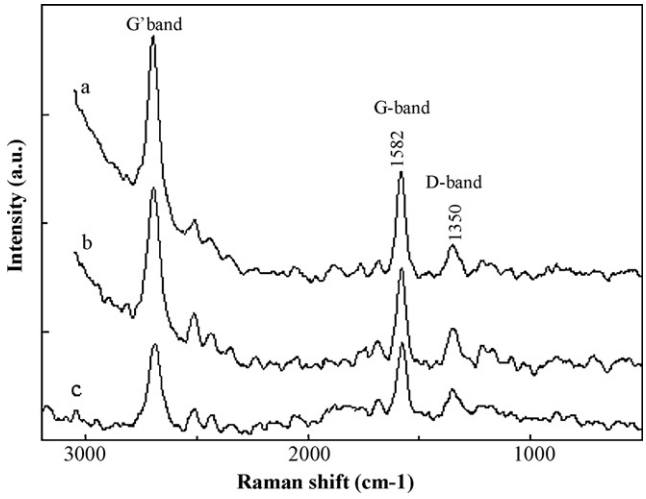

Fig. 8. Raman spectra of the CNTAZ samples with $x = 0.017$ (a), 0.034% (b) and 0.17% (c).

formed CNTs. SEM characterization of these tips in back scattered mode confirmed the possible presence of Fe/Fe_3C phase/s suggesting the existence of a tip-growth mechanism in charge of multi wall CNTs formation. Base-growth is generally initiated in case of the existence of strong interaction between substrate and the catalyst. Such mechanism has been reported in case of silicon substrates since silicon provides a very strong interaction with the catalyst via the formation of a metallic silicide phase [46,47]. Of course, when a barrier layer such as silicon oxide or titanium nitride is laid, the interaction between the substrate and the catalyst is weakened and tip growth is commonly observed [47]. Gohier et al. [48] have shown that in the early stage of the CNT nucleation, the first graphitic carbon chains formed on the surface of the large catalyst can quickly diffuse to the catalyst/substrate interface and stabilize it. This step leaves the top surface of the nanoparticles expressed for further carbon absorption. This nucleation step leads to the particle lift-off from the substrate. Once the connection with the substrate is broken, tip-growth is the only available growth mechanism. It should be also added that detailed TEM study of the CNTAZ samples prepared in this work also confirmed the presence of some iron particles inside the CNT bodies which indicates that during the growth process some iron was carried out of the support by the tube growth.

Moreover, microstructural analysis carried out by SEM and TEM on various CNTAZ samples also showed that the higher was the magnitude of x the lower was the concentration of CNT formation. This was also justified by carbon yield measurement as well. Fig. 10 demonstrates the carbon yield magnitudes of

Table 2
Characteristic Raman peaks intensities for various CNTAZ samples prepared in this work.

I_G/I_D	D-band	G-band	x
2.98	190	550	0.017
2.37	200	475	0.034
2	225	450	0.17

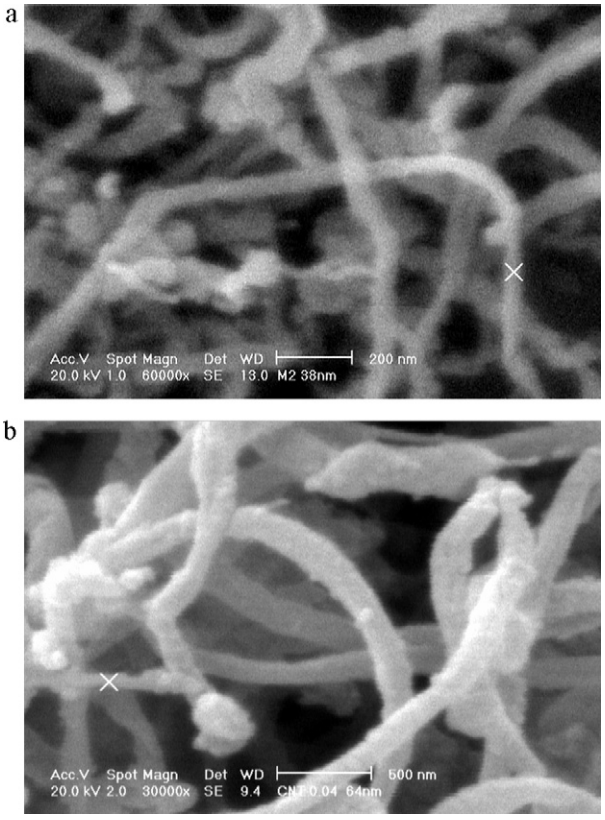

Fig. 9. (a and b) SEM micrographs of the CNTAZ sample with $x = 0.07$.

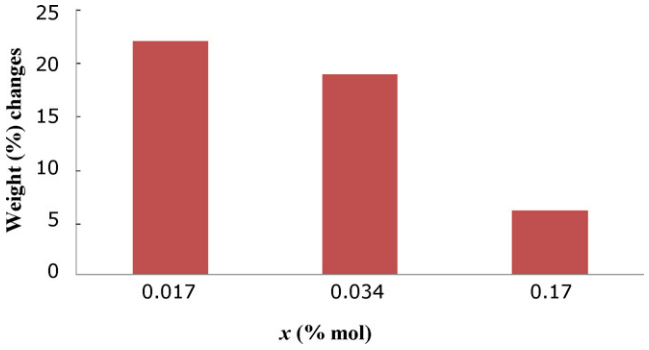

Fig. 10. Carbon yields of the various the CNTAZ prepared samples with different x.

the prepared samples versus the value of x. As can be noticed, increasing amounts of the initial iron content led to decreased carbon yield. The presence of lower carbon content for the samples with $x = 0.17$ denotes that the surface particles in these specimens could have been less active for the catalytic decomposition of CH_4 due to the formation of larger Fe/Fe_3 crystallite/grain sizes compared to the rest of the samples. In fact, in order to increase the yield of CNTs formation increasing numbers of active catalytic particles and prevention of their coalescence and growth on the matrix surface is required.

4. Conclusions

In the work presented here, we report successful synthesis of CNTAZ nanocomposite powders using solution combustion

and CVD methods. In this respect, ceramic nanocomposite precursors of $(Al_{2-x}Fe_xO_3)$–$(y)ZrO_2$ formula with $x = 0.017$, 0.034 and 0.17 and $y = 0.15$ were prepared. Further, during CVD process, in situ reduction of iron oxide to metallic iron (γ-Fe/α-Fe/Fe_3C) phase/s provided the necessary catalyst for the CNTs formation. The highest carbon yield was obtained for the sample with $x = 0.017$ for which the highest I_D/I_G ratio was detected reflecting the existence of higher level of structural order for this sample, based on Raman spectroscopy results.

Acknowledgements

We would like to acknowledge the support of Iranian Nanotechnology Initiative Council (INIC) and the kind help of Research Institute of Petroleum Industries (RIPI), Tehran, Iran.

References

[1] A. Peigney, Ch. Laurent, E. Flahaut, A. Rousset, Carbon nanotubes in novel ceramic matrix nanocomposites, Ceram. Int. 26 (2000) 677–683.
[2] M.F. Yu, O. Lourie, M.J. Dyer, K. Moloni, T.F. Kelly, R.S. Ruoff, Strength and breaking mechanism of multiwalled carbon nanotubes under tensile load, Science 287 (2000) 637–640.
[3] G. Van Lier, C. Van Alsenoy, V. Van Doren, P. Geerlings, Ab initio study of the elastic properties of single-walled carbon nanotubes and graphene, Chem. Phys. Lett. 326 (2000) 181–185.
[4] M.M.J. Treacy, T.W. Ebbesen, J.M. Gibson, Exceptionally high Young's modulus observed for individual carbon nanotubes, Nature 381 (1996) 678–680.
[5] R.H. Baughman, A.A. Zakhidov, W.A. de Heer, Carbon nanotubes—the route toward applications, Science 297 (2002) 787–792.
[6] M.J. Biercuk, M.C. Llaguno, M. Radosavlijevic, J.K. Hyun, A.T. Johnson, Carbon nanotube composites for thermal management, Appl. Phys. Lett. 80 (2002) 2767–2769.
[7] W.K. Maser, P. Bernier, J.M. Lambert, O. Stephan, P.M. Ajayan, C. Colliex, V. Brotons, J.M. Planeix, B. Coq, P. Molinié, S. Lefrant, Elaboration and characterization of various carbon nanostructures, Synth. Met. 81 (2/3) (1996) 243–250.
[8] Y. Ando, X. Zhao, H. Kataura, Y. Achiba, K. Kaneto, M. Tsuruta, S. Uemura, S. Iijima, Multiwalled carbon nanotubes prepared by hydrogen arc, Diamond Relat. Mater. 9 (2000) 847–851.
[9] T. Guo, P. Nikolaev, A. Thess, D.T. Colbert, R.E. Smalley, Catalytic growth of single-walled manotubes by laser vaporization, Chem. Phys. Lett. 243 (1/2) (1995) 49–54.
[10] V. Ivanov, A. Fonseca, J.B. Nagy, A. Lucas, P. Lambin, D. Bernaerts, X.B. Zhang, Catalytic production and purification of nanotubules having fullerene-scale diameters, Carbon 33 (12) (1995) 1727–1738.
[11] K. Hernadi, A. Fonseca, J.B. Nagy, D. Bernaerts, A.A. Lucas, Fe-catalyzed carbon nanotube formation, Carbon 34 (10) (1996) 1249–1257.
[12] K. Hernadi, A. Fonseca, J.B. Nagy, D. Bernaerts, J. Riga, A. Lucas, Catalytic synthesis and purification of carbon nanotubes, Synth. Met. 77 (1–3) (1996) 31–34.
[13] K. Hernadi, A. Fonseca, J.B. Nagy, A. Siska, I. Kiricsi, Production of nanotubes by the catalytic decomposition of different carbon-containing compounds, Appl. Catal. A: Gen. 199 (2) (2000) 245–255.
[14] A. Thaib, G.A. Martin, P. Pinheirob, M.C. Schouler, P. Gadelle, Formation of carbon nanotubes from the carbon monoxide disproportionation reaction over Co/Al_2O_3 and Co/SiO_2 catalysts, Catal. Lett. 63 (1999) 135–141.
[15] Y.H. Mo, A.K.M.F. Kibria, K.S. Nahm, The growth mechanism of carbon nanotubes from thermal cracking of acetylene over nickel catalyst supported on alumina, Synth. Met. 122 (2) (2001) 443–447.
[16] P. Chen, H.B. Zhang, G.D. Lin, Q. Hong, K.R. Tsai, Growth of carbon nanotubes by catalytic decomposition of CH_4 or CO on a Ni–MgO catalyst, Carbon 35 (10/11) (1997) 1495–1501.
[17] W. Merchan-Merchan, A.V. Saveliev, L. Kennedy, W.C. Jimenez, Combustion synthesis of carbon nanotubes and related nanostructures, Prog. Energy Combust. Sci. 36 (2010) 696–727.
[18] R.D. Purohit, B.P. Sharma, K.T. Pillai, A.K. Tyagi, Ultrafine ceria powders via glycine–nitrate combustion, Mater. Res. Bull. 36 (15) (2001) 2711–2721.
[19] A. Muan, C.L. Gee, Phase equilibrium studies in the system iron oxide-Al_2O_3 in air and at 1 atm pressure, J. Am. Ceram. Soc. 39 (1956) 207–214.
[20] A. Rousset, J. Paris, Formation des solutions solides binaires et ternaires des sesquioxydes de chrome. d'aluminium et de fer. III. Le syst'eme Fe_2O_3–Al_2O_3, Bull. Soc. Chim. Fr. 10 (1972) 3729–3733.
[21] C.E. Meyers, T.O. Mason, W.T. Petuskey, J.W. Halloran, H.K. Bowen, Phase equilibria in the system Fe–Al–O, J. Am. Ceram. Soc. 63 (1980) 659–663.
[22] X. Devaux, Ch. Laurent, A. Rousset, Chemical synthesis of metal nanoparticles dispersed in alumina, Nanostruct. Mater. 2 (1993) 339–346.
[23] S. Popovic, M. Ristic, S. Music, Formation of solid solution in the system Al_2O_3–Fe_2O_3, Mater. Lett. 23 (1995) 139–142.
[24] P. Tartaj, J. Tartaj, Microstructural evolution of iron-doped alumina nanoparticles synthesized from microemulsion, Chem. Mater. 14 (2002) 536–541.
[25] K. Tahmasebi, M.H. Paydar, The effect of starch addition on solution combustion synthesis of Al_2O_3–ZrO_2 nanocomposite powder using urea as fuel, Mater. Chem. Phys. 109 (1) (2008) 156–163.
[26] B.D. Cullity, S.R. Stock, Elements of X-ray Diffraction, second ed., Notre Dame, 1978.
[27] S.T. Aruna, K.S. Rajam, Mixture of fuels approach for the solution combustion synthesis of Al_2O_3–ZrO_2 nanocomposite, Mater. Res. Bull. 39 (2) (2004) 157–167.
[28] H. Gleiter, Nanostructured materials: basic concepts and microstructure, Acta Mater. 48 (1) (2000) 1–29.
[29] H.S. Nalwa, Nanostructured Materials and Nanotechnology, Academic Press, 2002.
[30] B. Mondal, A.B. Chattopadhyay, A. Virkar, A. Paul, Development and performance of zirconia-toughened alumina ceramic tools, Wear 156 (1992) 365–383.
[31] W.H. Tuan, R.Z. Chen, T.C. Wang, C.H. Cheng, P.S. Kuo, Mechanical properties of Al_2O_3/ZrO_2 composites, Eur. Ceram. Soc. 22 (16) (2002) 2827–2833.
[32] F.L. Matthews, R.D. Rawlings, Composite Materials: Engineering and Science, Chapman and Hall, London, 1994, p. 137.
[33] B. Kibbel, A.H. Heuer, Exaggerated grain growth in ZrO_2–toughened Al_2O_3, J. Am. Ceram. Soc. 69 (3) (1986) 231–236.
[34] D.J. Green, Critical microstructures for microcracking in Al_2O_3–ZrO_2 composites, J. Am. Ceram. Soc. 65 (12) (1982) 610–614.
[35] B. Fegley, P. White, H.K. Bowen, Preparation of zirconia–alumina powders by zirconium alkoxide hydrolysis, J. Am. Ceram. Soc. 68 (2) (1985) C-60–C-62.
[36] A.H. Heuer, Transformation toughening in ZrO_2-containing ceramics, J. Am. Ceram. Soc. 70 (10) (1987) 689–698.
[37] M.L. Balmer, F.F. Lange, V. Jayram, C.G. Levi, Development of nanocomposite microstructures in ZrO_2–Al_2O_3 via the solution precursor method, J. Am. Ceram. Soc. 78 (1995) 489–1494.
[38] R.C. Garvie, Stabilization of the tetragonal structure in zirconia microcrystals, J. Am. Chem. Soc. 82 (1978) 218.
[39] S. Ram, A. Mondal, X-ray photoelectron spectroscopic studies of Al^{3+} stabilized t-ZrO_2 of nanoparticles, Appl. Surf. Sci. 221 (1–4) (2004) 237–247.
[40] W.D. Kingery, H.K. Bowen, D.R. Uhlmann, Introduction to Ceramics, second ed., Wiley, New York, 1976.
[41] P. Coquay, E.D.E Grave, R.E. Vandenberghe, C. Dauwe1, E. Flahaut, C.H. Laurent, A. Peigney, A. Rousset, Mössbauer spectroscopy study of $MgAl_2O_4$-matrix nanocomposite powder containing carbon nanotubes and iron-based nanoparticles, Acta Mater. 48 (2000) 3015–3023.
[42] R. Sharma, E. Moore, P. Rez, M.M.J. Treacy, Site-specific fabrication of Fe particles for carbon nanotube growth, Nano Lett. 2 (2009) 689–694.

[43] R. Sharma, I. Zafar, In situ observations of carbon nanotube formation using environmental electron microscopy (ETEM), Appl. Phys. Lett. 84 (2004) 990–992.
[44] Z. Zhang, C. Dewan, S. Kothari, S. Mitra, D. Teeters, Carbon nanotubes synthesis, characteristics, and microbattery application, Mater. Sci. Eng. 116 (2005) 363–368.
[45] M.A. Ermakova, D. Yu Ermakov, A.L. Chuvilin, G.G. Kuvshinov, Decomposition of methane over iron catalysts at the range of moderate temperatures: the influence of structure of the catalytic systems and the reaction conditions on the yield of carbon and morphology of carbon filaments, J. Catal. 201 (2001) 83–197.
[46] C. Bower, O. Zhou, W. Zhu, D.J. Werder, S. Jin, Nucleation and growth of carbon nanotubes by microwave plasma chemical vapor deposition, Appl. Phys. Lett. 77 (2000) 2767–2769.
[47] G.S. Choi, Y.S. Cho, S.Y. Hong, J.B. Park, K.H. Son, D.J. Kim, Carbon nanotubes synthesized by Ni-assisted atmospheric pressure thermal chemical vapor deposition, J. Appl. Phys. 91 (2002) 3847–3854 (bottom of form).
[48] A. Gohier, C.P. Ewels, T.M. Minea, M.A. Djouadi, Carbon nanotube growth mechanism switches from tip- to base-growth with decreasing catalyst particle size, Carbon 46 (2008) 1331–1338.